Optical Determination of Electron-Phonon Coupling in Carbon Nanotubes

Y. Yin,[1] A. N. Vamivakas,[2] A. G. Walsh,[1] S. B. Cronin,[3] M. S. Ünlü,[2,1] B. B Goldberg,[1,2] and A. K. Swan[2]

[1]*Physics Department, Boston University, Boston, Massachusetts 02215, USA*

[2]*Electrical and Computer Engineering Department, Boston University, Boston, Massachusetts 02215, USA*

[3]*Electrical Engineering Department, University of Southern California, Los Angeles, California 90089, USA*

(Received 26 May 2006; published 19 January 2007)

We report on an optical method to directly measure electron-phonon coupling in carbon nanotubes by correlating the first and second harmonic of the resonant Raman excitation profile. The method is applicable to 1D and 0D systems and is not limited to materials that exhibit photoluminescence. Experimental results for electron-phonon coupling with the radial breathing mode in 5 different nanotubes show coupling strengths from 3–11 meV. The results are in good agreement with the chirality and diameter dependence of the *e*-ph coupling calculated by Goupalov *et al.*

DOI: 10.1103/PhysRevLett.98.037404 PACS numbers: 78.67.Ch, 63.22.+m, 73.63.Fg, 78.30.−j

The intrinsic coupling between the electronic and atomic degrees of freedom is fundamental to many transport and optical properties of condensed matter. Here we examine carbon nanotubes, a prototypical one-dimensional (1D) system under intense study to understand both their fundamental physical properties and their potential applications as transistors, sensors, and optoelectronic devices. The electron-phonon (*e*-ph) coupling in carbon nanotubes (CNTs) is a key coupling parameter in the electronic band structure as it controls Raman scattering [1], heat and electron conductivity [2], and sets an upper limit to ballistic transport [3,4]. In polar semiconductors, multiphonon replicas in luminescence have been used to measure the Fröhlich *e*-ph coupling with longitudinal optical (LO) phonons in good agreement with theory [5,6]. In low dimensional systems, the electron and phonon confinement complicates the situation, with conflicting experimental results [7], and requiring model-dependent interpretation to extract the *e*-ph interaction. *E*-ph interactions in CNTs are due to the deformation-potential interaction, generally weaker than Fröhlich interaction in polar materials. Nonetheless, evidence of *e*-ph coupling in CNTs are observed in photoluminescence phonon replicas [8], the Kohn anomaly manifested in the phonon dispersion and line widths in metallic nanotubes [9] and temperature dependence of optical transition energies [10,11]. However, direct measurements of *e*-ph coupling in CNTs are lacking.

Recent tight-binding calculations predict a strong chirality and family dependence of the *e*-ph coupling of the radial breathing mode (RBM) in carbon nanotubes [12,13]. The relative strengths of the *e*-ph couplings are supported by Raman intensity measurements from a CNT ensemble, assuming a uniform chirality distribution [12]. Generally, both optical and transport ensemble measurements are complicated by the variation of electronic and phonon structure with chirality within the ensemble, and single tube measurements have provided advancements with the knowledge of the (n, m) structure [2,14–17]. In this Letter, we extract an absolute value of the RBM *e*-ph coupling by comparing the Raman intensity of the RBM mode and its overtone. Our general approach is enabled by using the full resonant Raman profile, thus simply accounting for contributions from the optical matrix elements, resonant enhancement factors, and collection and detection efficiencies. The results accurately follow the chiral dependence suggested from calculations [12].

We investigate a series of singly optically resonant single wall carbon nanotubes (SWNTs) of different diameters and chiralities, grown by chemical vapor deposition over 1–1.5 μm wide trenches etched in quartz substrates [10]. The inset in Fig. 1(a) shows a scanning electron microscopy (SEM) picture of the small bundles of a typical sample. While occasionally more than one nanotube is resonant in the focused laser beam (~0.5 μm), we deliberately choose only singly resonant tubes for this study. A

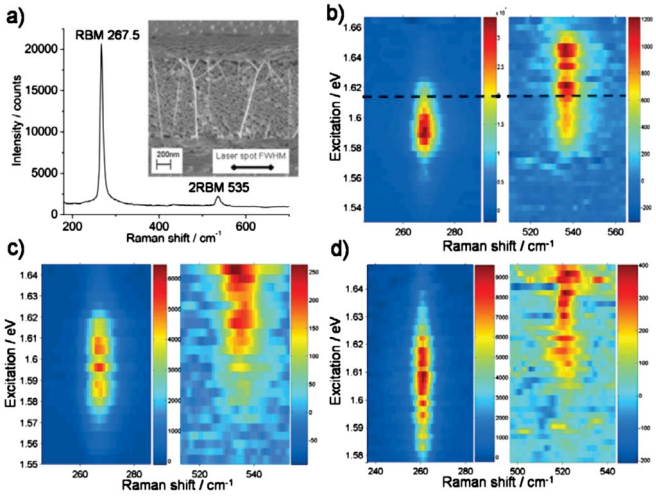

FIG. 1 (color). (a) A Raman spectrum of CNT (11,0) under the excitation energy 1.615 eV and a SEM picture (inset) of the sample showing small, suspended bundles compared with the laser spot size. (b)–(d) 2D color maps of resonant Raman scattering excitation spectra of RBM and 2RBM of a singly resonant tube. (b) Spectra for (11,0) tube with 3-point smoothing. The line cut indicates the spectrum in (a) (tube 5 in Table I); (c) (11,0) tube (tube 5' in Table I); (d) (10,2) tube (tube 4 in Table I).

TABLE I. A list of measured SWNTs with their RBM $|M_{e\text{-ph}}|$ values and assignments. The $|M_{e\text{-ph}}|^2$ value for the (9,7) SWNT is determined by comparing the ratio of the first and second order RRSE of another mode, M273, to the RBM because the 2RBM is too weak to be measured for (9,7). $|M_{e\text{-ph}}|$ values for phonon modes other than RBM will be further discussed in a separate publication. CNT 5' is a remeasurement of CNT 5.

	ω_{RBM}	n, m	d_t (nm)	θ (°)	ν	w_Γ	E_{22} (eV)	η (meV)	A	A' ($\times 10^{-5}$)	$\lvert M_{e\text{-ph}}\rvert^2 \times 10$ (meV^2)	$\lvert M_{e\text{-ph}}\rvert$ (meV)
1	206.0	14,1	1.153	3.42	1	1	1.567	14	2 ± 2	6.3 ± 3	3 ± 4	5 ± 4
2	219.0	9,7	1.103	25.87	-1	1	1.554	38	0.3 ± 0.2	N/A	0.9 ± 0.6	3 ± 1
3	259.0	9,4	0.916	17.48	-1	1	1.627	19	6 ± 2	41 ± 9	5 ± 2	7 ± 1
4	260.5	10,2	0.884	8.95	-1	1	1.591	16	1.7 ± 0.6	24 ± 4	10 ± 4	10 ± 2
5	267.5	11,0	0.873	0	-1	0.8	1.576	14	4 ± 1	56 ± 6	13 ± 4	11 ± 2
5′	267.0	11,0	0.873	0	-1	0.8	1.579	13	0.9 ± 0.3	13 ± 2	13 ± 4	11 ± 2

high throughput micro-Raman system with excitation range from 720–830 nm is used [18]. Powers less than 2 mW in a 0.5 μm spot size avoid tube heating [10,18], and the different Raman modes are collected simultaneously for each excitation energy.

Figures 1(b)–1(d) show the intensity maps of the resonant Raman scattering excitation (RRSE) signal of the RBM and two-phonon RBM overtone (2RBM) for three different nanotubes. Figure 1(a) shows a single Raman spectrum (RBM = 267.5 cm^{-1}, 2RBM = 535 cm^{-1}) and Fig. 1(b) shows the full 2D spectral data map for the same tube after subtracting a linear background. The 2RBM peak is much weaker, and the resonance is shifted by one phonon energy to higher excitation energy due to the two-phonon resonant enhancement process. Similar intensity maps are shown for two other nanotubes with RBM (267 cm^{-1}) and 2RBM (534 cm^{-1}) Fig. 1(c), and RBM (260.5 cm^{-1}) and 2RBM (521 cm^{-1}) in Fig. 1(d). The resulting RRSE profiles from the RBM and 2RBM peaks in Fig. 1(b) are shown in Fig. 2 as well as a profile of the anti-Stokes one-phonon RBM. We use standard perturbation theory [19] to fit the one- and two-phonon RRSE profiles and correlate the profiles to extract the absolute value of e-ph coupling matrix elements.

The resonant Raman cross section for first order, one-phonon scattering is given by [19,20]

$$\frac{d_1\sigma'(E_L, E_{\mathrm{ph}}, \theta)}{d\Omega} = A\frac{(E_L - E_{\mathrm{ph}})^2}{E_{\mathrm{ph}}^2 E_L^2}\left|\frac{1}{\sqrt{E_L - E_{ii} - i\eta}} - \frac{1}{\sqrt{E_L - E_{\mathrm{ph}} - E_{ii} - i\eta}}\right|^2, \quad (1)$$

where we define $A = CN_{\mathrm{ph}}|M_{e\text{-ph}}|^2$. C is a tube-dependent constant which includes the photon energy independent parts of the optical matrix elements. In our calculation, only one electron and hole band with a transition energy E_{ii} are considered [21]; E_L is the excitation photon energy; E_{ph} is the phonon energy; η is the broadening factor in units of energy. $M_{e\text{-ph}}$ is the e-ph transition matrix element; $N_{\mathrm{ph}} = (n_{\mathrm{ph}} + 1)$ for Stokes scattering and $N_{\mathrm{ph}} = n_{\mathrm{ph}}$ for anti-Stokes scattering, where $n_{\mathrm{ph}} = 1/(e^{|E_{\mathrm{ph}}|/kT} - 1)$ is the phonon number. Only zone center (Γ point) phonons are involved in one-phonon first order Raman processes, so $M_{e\text{-ph}}$ is the e-ph coupling at the Γ point. Equation (1) is used to fit the RBM resonant excitation profiles, obtain the values of A, E_{ii}, and η for a particular phonon mode of a particular SWNT and calculate the anti-Stokes resonant Raman profiles.

Two-phonon scattering is more complex and includes both simultaneous and sequential emission [19], though under normal phonon densities it is believed that simultaneous emission is negligible [22]. The strong two-phonon RRSE scattering we observe at the intermediate state $E_{ii} + E_{\mathrm{ph}}$, which doesn't exist in simultaneous emission, supports this assumption. In our calculation then, we consider only the sequential emission of two phonons. Two-phonon Raman scattering lifts the Γ point restriction of one-phonon scattering since two phonons with opposite wave vectors satisfy momentum conservation for an optical process. This allows non-Γ point phonons to mediate the scattering process and thus makes possible the observation of scattered photon energies that are not simply twice the energies observed in one-phonon Raman scattering. In our measured two-phonon Raman spectra we observe one two-

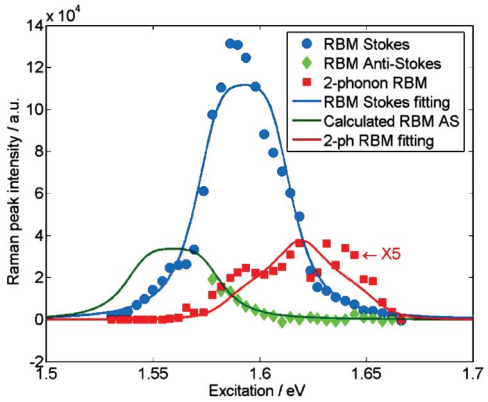

FIG. 2 (color). CNT (11,0) RBM, 2-phonon RBM and anti-Stokes RBM resonant excitation profiles. The data and curves for anti-Stokes, Stokes, and two-phonon RBM are presented by green (diamond), blue (dot), and red (square) marks. The blue curve fits Eq. (1) to the Stokes RBM RRSE and the green curve is the calculated anti-stokes RRSE. The red curve fits Eq. (2) to the two-phonon RBM RRSE (×5).

phonon peak at 2 × RBM frequency [Fig. 1(b)], indicating a dominant contribution from phonons near the Γ point. Because of the allowance of non-Γ phonon transitions, 2RBM peaks show a broader linewidth and an asymmetric line shape extending to high phonon energy direction. To determine the spectral weight of the contribution from the phonons near the Γ point, we require the density of states (DOS) of the particular CNT phonon mode. We calculate the DOS from the phonon dispersion using a microscopic mass and spring model of the nanotube lattice dynamical properties first developed by Mahan and Jeon for achiral tubes and later extended to chiral SWNTs [23]. Not surprisingly, we find that the DOS has a strong singularity at the Γ point. For the higher symmetry (11,0) tube, the calculation shows an additional singularity at the zone boundary. Using the RBM DOS $\rho_{\mathrm{DOS}}^{\mathrm{RBM}}(\Omega)$ we determine the spectral weight from the Γ point, $w_\Gamma = \int \rho_{\mathrm{DOS}}^{\mathrm{RBM}}(\Omega) d\Omega$ where the integration extends over the Γ point singularity, and where the integral of DOS over the entire frequency range is normalized to unity. Our calculation shows that $w_\Gamma \approx 1$ for RBM in chiral SWNTs, while $w_\Gamma = 0.8$ for the achiral (11,0) CNT. Since the contribution to the phonon DOS at the Γ point comes from a small range of q values, we approximate the RBM DOS as a delta function weighted by w_Γ. Then, the Γ point phonon contribution to the two-phonon Raman scattering cross section can be described as

$$\frac{d_1\sigma'(E_L, E_{\mathrm{ph}}, \theta)}{d\Omega} = A' \frac{(E_L - 2E_{\mathrm{ph}})^2}{E_L^2} \times \left| \frac{(p_1 + p_2 + p_3)}{(p_1 + p_3)(p_1 + p_2)(p_3 + p_2)} \cdot \frac{1}{p_1 p_2 p_3} \right|^2, \quad (2)$$

where we define $p_j = \sqrt{E_L - E_{ii} - (j-1)E_{\mathrm{ph}} - i\eta}$, $j = 1, 2, 3$, and $A' = CN_{\mathrm{ph}}^2 |M_{e\text{-ph}}|^4 w_\Gamma$. C is the same constant used in the one-phonon scattering [Eq. (1)]. Approximating the RBM DOS does not effect A' but we expect that a slight asymmetry in the line shape and marginally higher E_{ii}, effects are missed by this treatment.

The simultaneous measurement of the one-phonon and two-phonon resonant Raman profile spectra for a single mode, such as the RBM, allows us to directly determine the e-ph coupling for the Γ point phonons. We fit the experimental results with Eqs. (1) and (2) to obtain A and A' and use Eq. (3) to obtain the absolute values of e-ph coupling matrix elements

$$|M_{e\text{-ph}}|^2 = \frac{A'/w_\Gamma}{AN_{\mathrm{ph}}}. \quad (3)$$

The RBM profile for the (11,0) CNT in Fig. 2 is fit with Eq. (1) to obtain the A, E_{ii} (here E_{ii} is E_{22}), and η values. Our tube assignment of (11,0) is based on its RBM frequency (ω_{RBM}) and E_{22} transition energy [18,24,25]. The SWNT's diameter (d_t), chiral angle (θ), and chiral index $\nu = \mathrm{mod}(n - m, 3)$ are also obtained from the assignment. The two-phonon RBM excitation profile for (11,0) is fit with Eq. (2) and also plotted in Fig. 2. In the fitting of the two-phonon RRSE profile, the broadening factor η is fixed at the value from the corresponding one-phonon scattering. The parameter E_{ii} is allowed to vary independently and is, as expected, slightly larger (~10 meV) than E_{22} due to the approximation in Eq. (2) using a delta-function RBM DOS at the Γ point. Next, the value of $|M_{e\text{-ph}}|^2$ is obtained from Eq. (3) using the calculated w_Γ value. Quantitative values for (11,0) are listed in Table I. Errors in $|M_{e\text{-ph}}|^2$ are calculated from fitting errors of A and A', which are assumed to be uncorrelated. RRSE measurements are performed on four additional, different SWNTs: (10,2), (9,4), (9,7), and (14,1). The assignments, profile fitting results, and measured RBM $|M_{e\text{-ph}}|$ values are listed in Table I.

The dependence of RBM e-ph coupling strength is a strong function of the SWNT's diameter, chiral angle, and chiral index. Based on their tight-binding calculation [12], Goupalov, *et al.* proposed that e-ph coupling for RBM in SWNTs has a form

$$|M_{e\text{-ph}}|^2 = \left| \frac{a}{d_t^2} + \nu \frac{b}{d_t} \cos 3\theta \right|^2, \quad (4)$$

where the constants a and b depend on which electronic energy level E_{ii} is excited. The ratio b/a has negative sign for E_{22}, resulting in a stronger e-ph coupling for $\nu = -1$. Our experimental data are fit remarkably well ($R^2 = 0.996$) by Eq. (4), with $a = 1.8 \pm 0.4$ (meV · nm^2) and $b = -7.7 \pm 0.5$ (meV · nm) for our in-rope SWNTs under E_{22} resonance. The errors of a and b are determined by fitting with a 0.95 confidence level. The ratio of $|b/a| = 4.3$ nm^{-1} is slightly larger than the theoretical value $|b/a| = 3/(5a_0) = 4.2$ nm^{-1} [12] using $a_0 = 0.142$ nm. The fitting result from Eq. (4) is plotted as a color map in Fig. 3(a) ($\nu = -1$) and Fig. 3(b) ($\nu = 1$) as a function of chiral angle and tube diameter together with colored squares in front showing our measured values. Figure 3(c) shows the same results plotted vs diameter to more accurately display the difference between the fit and our data. The coupling strength [Eq. (4)] has a node for $\nu = 1$ shown in Fig. 3(b), which agrees with a prediction made by J. Jiang *et al.* using the tight-binding approximation [26]. Later work by the same group [13] using an extended tight-binding approximation found similar dependence on diameter and angle, also in agreement with Ref. [12] and our data. In addition, the values of the measured e-ph coupling strengths can be compared with *ab initio* calculations by M. Machon *et al.* [27]. The *ab initio* e-ph coupling result for the (11,0) tube is larger (28 meV) than our measured value (11 ± 2 meV). We attribute this discrepancy to the difference in e-ph coupling strength between isolated SWNTs and SWNTs in bundles, to be examined in a separate publication.

These results confirm that the e-ph coupling is well described by the deformation-potential interaction derived

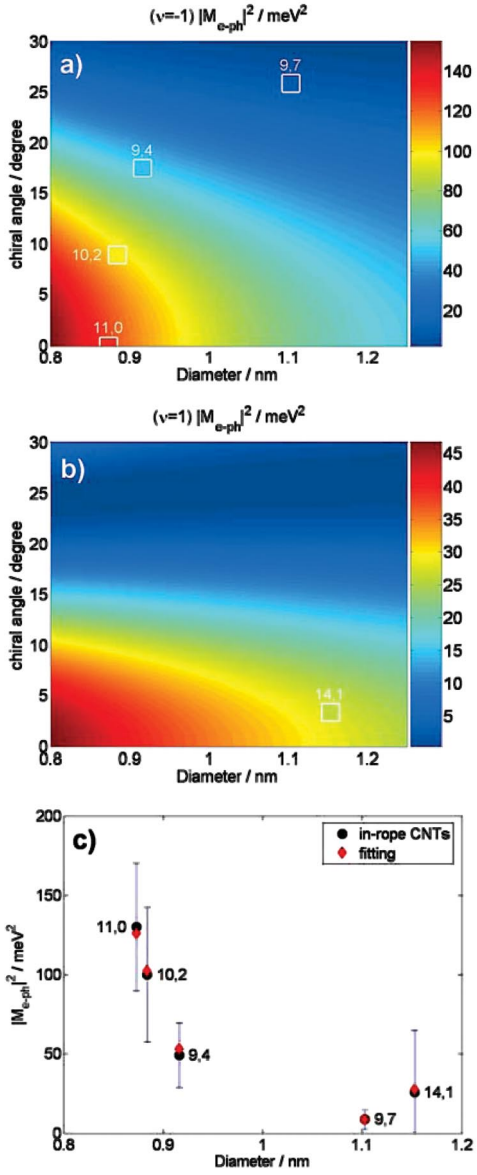

FIG. 3 (color). Measured $|M_{e\text{-ph}}|^2$ values for 5 in-rope SWNTs and the fitting result with Goupalov's formula. (a) and (b) are color-map plots of $|M_{e\text{-ph}}|^2$ as a function of chiral angle and diameter for SWNTs with chiral index $\nu = -1$ and $\nu = 1$; the background colors are the fitted results while measured values are presented as color squares on top with the same color-map scales. (c) plots the $|M_{e\text{-ph}}|^2$ vs diameter for measured values (black dots) with error bars and fitted results (red diamonds).

from the empirical tight-binding model. The results demonstrate that the interference of the chirality-dependent and chirality-independent terms indeed lead to stronger interactions for $\nu = -1$ carbon nanotubes at E_{22}, in agreement with the many experimental studies that observe stronger Raman cross sections $\nu = -1$ for E_{22} transitions. Practically, this means that ensemble Raman measurements must be appropriately scaled to extract the chirality distribution.

In summary, we have proposed and demonstrated an optical method for the direct measurement of e-ph coupling $|M_{e\text{-ph}}|$ in carbon nanotubes. By correlating the full resonant Raman excitation profiles of the first and second harmonic of the radial breathing mode and accounting for the phonon density of states, we determine the e-ph coupling strengths for SWNTs under E_{22} resonance for five singly resonant SWNTs in small ropes. The results agree with calculated functional dependence of e-ph coupling on chiral angle, tube diameter, and chiral index ν. This technique does not require luminescence and could be applied to any low dimensional (1D or 0D) system, e.g., nanorods and quantum dots—systems which exhibit strong electronic resonance enhancements and well-defined phonon lines.

[1] M. S. Dresselhaus *et al.*, Phys. Rep. **409**, 47 (2005).
[2] Z. Yao, C. L. Kane, and C. Dekker, Phys. Rev. Lett. **84**, 2941 (2000).
[3] V. Perebeinos, J. Tersoff, and P. Avouris, Phys. Rev. Lett. **94**, 086802 (2005).
[4] J. Y. Park *et al.*, Nano Lett. **4**, 517 (2004).
[5] K. Huang and A. Rhys, Proc. R. Soc. A **204**, 406 (1950).
[6] X. B. Zhang *et al.*, J. Phys. Condens. Matter **13**, 7053 (2001).
[7] S. Nomura and T. Kobayashi, Phys. Rev. B **45**, 1305 (1992); V. M. Fomin *et al.*, Phys. Rev. B **57**, 2415 (1998); S. Schmitt-Rink, D. A. B. Miller, and D. S. Chemla, Phys. Rev. B **35**, 8113 (1987); J. J. Shiang, S. H. Risbud, and A. P. Alivisatos, J. Chem. Phys. **98**, 8432 (1993).
[8] S. G. Chou *et al.*, Phys. Rev. Lett. **94**, 127402 (2005).
[9] M. Lazzeri *et al.*, Phys. Rev. B **73**, 155426 (2006).
[10] S. B. Cronin *et al.*, Phys. Rev. Lett. **96**, 127403 (2006).
[11] J. Lefebvre, P. Finnie, and Y. Homma, Phys. Rev. B **70**, 045419 (2004).
[12] S. V. Goupalov, B. C. Satishkumar, and S. K. Doorn, Phys. Rev. B **73**, 115401 (2006).
[13] J. Jiang *et al.*, Phys. Rev. B **72**, 235408 (2005).
[14] M. Y. Sfeir *et al.*, Science **306**, 1540 (2004).
[15] J. Lefebvre *et al.*, Phys. Rev. B **69**, 075403 (2004).
[16] X. J. Zhou *et al.*, Phys. Rev. Lett. **95**, 146805 (2005).
[17] J. C. Meyer *et al.*, Phys. Rev. Lett. **95**, 217401 (2005).
[18] Y. Yin *et al.*, IEEE J. Sel. Top. Quantum Electron. **12**, 1083 (2006).
[19] R. M. Martin and L. M. Falicov, *Light Scattering in Solids I*, (Springer, New York, 1975), Vol. 8, Chap. 3.
[20] M. Canonico *et al.*, Phys. Rev. B **65**, 201402(R) (2002).
[21] The shape of the resonance Raman profile is nearly identical to that of a strongly bound exciton. A. N. Vamivakas *et al.*, Phys. Rev. B **74**, 205405 (2006).
[22] R. Al-Jishi and G. Dresselhaus, Phys. Rev. B **26**, 4514 (1982).
[23] G. D. Mahan and G. S. Jeon, Phys. Rev. B **70**, 075405 (2004); W. Mu and Z.-c. Ou-Yang, cond-mat/0512570.
[24] C. Fantini *et al.*, Phys. Rev. Lett. **93**, 147406 (2004).
[25] J. Maultzsch *et al.*, Phys. Rev. B **72**, 205438 (2005).
[26] J. Jiang *et al.*, Phys. Rev. B **71**, 205420 (2005).
[27] M. Machon *et al.*, Phys. Rev. B **71**, 035416 (2005).